AIMS Biophysics

AIMS Biophysics, 13(3): 287−301.
DOI: 10.3934/biophy.2026017
Received: 15 May 2026
Revised: 07 July 2026
Accepted: 15 July 2026
Published: 31 July 2026

http://www.aimspress.com/journal/biophysics

*Research article*

# The pRNA-assisted RNA imaging scheme (pARIS): a generalizable scaffold-based approach to facilitate cryo-EM structure determination of small RNAs

**Seth Scott[1], Nikolai Prokhorov[1,2], Wei Zhao[3], Paul J. Jardine[3], Marc C. Morais[1,2,*] and Kyung H. Choi[1,2,*]**

[1] Department of Biochemistry and Molecular Biology, Sealy Center for Structural Biology, The University of Texas Medical Branch, Galveston, TX 77555, USA
[2] Department of Molecular and Cellular Biochemistry, Indiana University, Bloomington, IN 47405, USA
[3] Department of Diagnostic and Biological Sciences, School of Dentistry, and Institute for Molecular Virology, University of Minnesota, Minneapolis, MN 55455, USA

* **Correspondence:** Email: mcmorais@iu.edu, kaychoi@iu.edu.

**Abstract:** RNA performs diverse biological functions that are often encoded in its three-dimensional structure. However, RNA-only structures represent a small fraction (~1%) of entries in the Protein Data Bank (wwPDB), limiting our knowledge of RNA structure–function relationships. The ribose-phosphate backbone of RNA is relatively flexible compared to proteins and typically forms weaker long-range tertiary interactions, resulting in structures that are less amenable to X-ray crystallography than folded proteins. Further, many functional RNAs range from 50 to 200 nt in size and are often too small for structure determination by cryo electron microscopy (cryo-EM). To facilitate RNA structure determination by cryo-EM, we present the procapsid RNA (pRNA)-assisted RNA imaging scheme (pARIS). In this approach, the RNA of interest is fused to the pRNA of bacteriophage Φ29 to enhance stability and reduce sample heterogeneity. The pRNA-linked RNA is then assembled onto the Φ29 procapsid to form a stable pentameric complex. This approach increases effective molecular mass, improves signal-to-noise ratio, and facilitates particle picking and alignments during cryo-EM imaging processing. Using pARIS, we determined a 4.8 Å structure of a 70 nt (~23 kDa) tRNA as proof of principle and a 6.7 Å structure of the liver-specific host microRNA-122 bound to its target site in the hepatitis C virus genome, demonstrating applicability to biologically relevant RNA targets.

**Keywords:** cryogenic electron microscopy; cryo-EM; RNA structure; RNA scaffold; bacteriophage Φ29; pRNA; pRNA scaffold; tRNA; HCV 5' UTR; miR-122

## 1. Introduction

While more than 80% of the genome is transcribed, only 1%–2% of transcripts encode proteins [1−3]. Accordingly, the number of annotated non-coding RNAs continues to grow, revealing an expanding repertoire of functional RNA molecules [4,5]. In non-coding RNAs, function is often encoded not in sequence per se but in three-dimensional structure, enabling roles in catalysis, gene regulation, and molecular recognition [6−8]. This is particularly evident in RNA viruses, whose genomes contain extensive secondary and tertiary structural elements that are essential for viral replication, translation, and host interactions. Therefore, a deeper understanding of RNA structure has the potential to inform new RNA-based antiviral strategies [9].

Despite the growing recognition of RNA function, our knowledge of RNA structure lags far behind that of proteins. Compared to proteins, RNA exhibits greater conformational heterogeneity due to the flexibility of its ribose-phosphate backbone and generally weaker long-range tertiary interactions, complicating structural analysis [10]. Although over 230,000 protein structures are deposited in the wwPDB, only ~2100 RNA-only structures are currently available, with relatively few new structures reported each year. Moreover, most solved RNA structures correspond to very large assemblies, such as the ribosome, or to small RNA duplexes, leaving a substantial gap in the structural characterization of functionally important medium-sized RNAs (~50–200 nt; ~16.5–66 kDa).

Advances in cryo electron microscopy (cryo-EM) single-particle analysis (SPA) have expanded the range of macromolecules amenable to structural studies, including increasingly small protein and RNA complexes. However, RNA remains a challenging target due to its size, intrinsic flexibility, and the lack of RNA-specific processing pipelines. In RNA crystallography, fusion strategies have been used to stabilize target RNAs and facilitate structure determination [11−15]. By incorporating RNAs of interest into well-behaved scaffolds, these approaches reduce conformational heterogeneity and improve the likelihood of crystallization. Here, we extend this concept to cryo-EM by developing a fusion-based strategy that we term procapsid RNA (pRNA)-assisted RNA imaging scheme (pARIS). This approach uses the bacteriophage Φ29 pRNA as a scaffold to stabilize an RNA of interest and enhance its visibility in cryo-EM.

The Φ29 DNA packaging motor consists of a connector protein, pRNA, and an ATPase and packages the viral genome into a preformed procapsid [16−18]. Structural studies have shown that five copies of pRNA assemble into a stable pentamer at the unique procapsid vertex where the connector resides and the ATPase ring assembles [19,20]. In pARIS, the RNA of interest is fused to a minimal procapsid-binding domain of pRNA and assembled onto the preformed Φ29 procapsid. This creates a stable, symmetry-defined complex that increases the effective molecular mass of the RNA and facilitates particle alignment and reconstruction in cryo-EM. The pRNA-fused RNA is visualized in the context of the procapsid, and the structure of the attached RNA is determined using focused reconstruction approaches. Using this strategy, we determined the structure of human tRNA as proof of principle and the structure of a biologically relevant RNA complex formed by the hepatitis C virus (HCV) 5' untranslated region (UTR) and the liver-specific host microRNA-122 (miR-122). These results demonstrate that pARIS provides a practical and generalizable approach for extending cryo-

EM structure determination to smaller and more flexible RNA molecules.

## 2. Methods

### *2.1. Design of pRNA constructs*

The Φ29 pRNA procapsid-binding domain (nt 25-95) was used as a scaffold to attach target RNAs, based on the pRNA structure (PDB: 3R4F) [21]. The native pRNA places both the 5′ and 3′ termini at one end of the molecule. Direct fusion of a target RNA at these termini could introduce flexibility, as the target RNA is linked through a single-stranded connection that allows rotational freedom. To reduce this flexibility, we designed a circularly permuted pRNA (pRNAcp), in which the 5′ and 3′ termini were relocated to the procapsid-binding region [22]. The tRNA sequence (70 nt) was inserted between positions 58 and 128 of the permuted pRNA scaffold. For the HCV: miR-122 construct, we used the wild-type pRNA. The first 29 nt of the HCV genome (genotype 1a) were appended to the 5′ end of pRNA, and the 24 nt miR-122 sequence was appended to the 3′ end. This design allows the fused RNA to fold, so that the HCV and miR-122 sequences are positioned proximally upon folding of the pRNA scaffold.

### *2.2. T7 RNA transcription and purification of pRNA-linked target RNAs*

pRNA-fused tRNA and HCV: miR-122 RNAs were generated by in vitro T7 transcription. The pRNA-fused HCV: miR-122 construct was assembled from two DNA oligonucleotides: a forward oligo containing the first 73 nt and a reverse oligo containing the reverse complement of the final 74 nt, with a 28 nt overlap (Table S1). The oligos were mixed at 20 nM and extended using Phusion DNA polymerase (New England Biolabs) to generate a double-stranded DNA template. PCR amplification was performed using primers (200 nM), with the forward primer containing the T7 promoter sequence. The resulting PCR product was used as a template for in vitro transcription with T7 RNA polymerase. The transcribed RNA was purified by anion exchange chromatography using a MonoQ column with a 0–500 mM NaCl gradient. Fractions containing the pRNA-fused RNA were pooled, buffer-exchanged to 20 mM Tris-HCl (pH 7.4), 100 mM NaCl, and 2 mM $MgCl_2$, and concentrated to 1 mg/mL. Purity was assessed by denaturing 10% PAGE containing 8 M urea.

### *2.3. Cryo-EM sample preparation and data acquisition*

Φ29 procapsids were generated using an amber mutant as previously described [23,24]. Φ29 procapsids and pRNA-fused RNAs were mixed to assemble pRNA-bound procapsids. The RNA was diluted to 1.2 μM in 0.5× TM buffer (25 mM Tris, 5 mM $MgSO_4$, pH 7.5), heated to 60 °C for 2 min, and cooled on ice for 10 min. Five microliters of RNA was mixed with 5 μL of 0.5× TM buffer containing 0.06 μM procapsids, corresponding to a 20:1 molar ratio of pRNA to procapsid. The mixture was incubated on ice for an additional 10 min prior to grid preparation. Samples were applied to glow-discharged Quantifoil R2/1 (200 mesh) grids, incubated for 40 s, blotted for 17 s using a Leica EM GP2 plunge freezer, and vitrified in liquid ethane. Initial screening was performed on a JEOL JEM 2100 microscope. Grids suitable for data collection were imaged on a Thermo Fisher Titan Krios equipped with a Gatan K3 detector. Additional data collection and processing parameters are

listed in Supplementary Table S2.

### *2.4. Image processing and reconstruction*

Cryo-EM data for both the pRNA–tRNA and pRNA–HCV: miR-122 constructs were processed in cryoSPARC [25]. Briefly, motion correction, CTF estimation, particle picking, and initial 2D classification were performed using standard procedures. Particles were subjected to 3D refinement of the procapsid, after which the pRNA vertex was identified, and particles were recentered and reextracted into a smaller box. Fivefold symmetry expansion was then performed, followed by signal subtraction to isolate individual pRNA-linked RNA copies from the pentameric assembly. Focused classification and local refinement were subsequently used to improve reconstruction of the target RNA. Final maps were post-processed using DeepEMhancer [26]. Key processing parameters, particle numbers, and refinement procedures for each dataset are summarized in Supplementary Table S2. Additional details of classification strategies and reconstruction workflow are described in the Results section.

### *2.5. Model fitting of the pRNA-tRNA and pRNA-HCV: miR-122 complex*

The cryo-EM density for pRNA-tRNA was used to fit structures of the pRNA (PDB: 3R4F) and the tRNA (PDB: 1EXD) with a minor adjustment of the angle between the acceptor stem and the D arm, as this angle can vary between tRNA structures. Since the overall fit was otherwise good, no additional model adjustments were performed. The cryo-EM density corresponding to the HCV: miR-122 complex was used to fit structures of the pRNA (PDB: 3R4F) and the HCV: miR-122 complex (PDB: 7KI3). Because the crystal structure did not fully account for the observed density, individual regions were fitted as rigid bodies, including terminal base pairs, SLI, and the proximal duplex region. The fitted models were manually adjusted using the real-space refinement tools in Coot to improve agreement with the EM density. [27]. The 3′ overhang of miR-122 (6 nts) was excluded from the model due to the lack of interpretable density.

The cryo-EM density maps have been deposited at the Electron Microscopy Data Bank (EMDB) under accession codes EMD-77966 (pRNA-tRNA) and EMD-77925 (pRNA-HCV: miR-122 complex). The corresponding atomic coordinates for the pRNA-HCV: miR-122 complex have been deposited at the Protein Data Bank (PDB) under accession code 36WR.

## 3. Results

### *3.1. Overview of pARIS*

The goal of pARIS is to enable structural analysis of small RNA molecules by overcoming limitations associated with their size and conformational flexibility. To achieve this, we use the bacteriophage Φ29 pRNA as a scaffold to attach RNAs of interest to a large viral capsid. Fusing an RNA of interest to the pRNA stabilizes the target RNA and increases its effective size. Additionally, the resulting pRNA-RNA fusion construct recognizes and binds to a unique fivefold vertex of the procapsid, where it assembles into a stable pentameric ring via intermolecular base pairs between adjacent pRNAs [21]. To determine the structure of the target RNA, the entire viral procapsid structure

is first reconstructed. Densities corresponding to the pRNA-linked RNA are then reextracted into a smaller box, and the structure of the target RNA is determined by C5 symmetry expansion followed by focused refinement of a single RNA. The overall workflow of pARIS is shown in Figure 1.

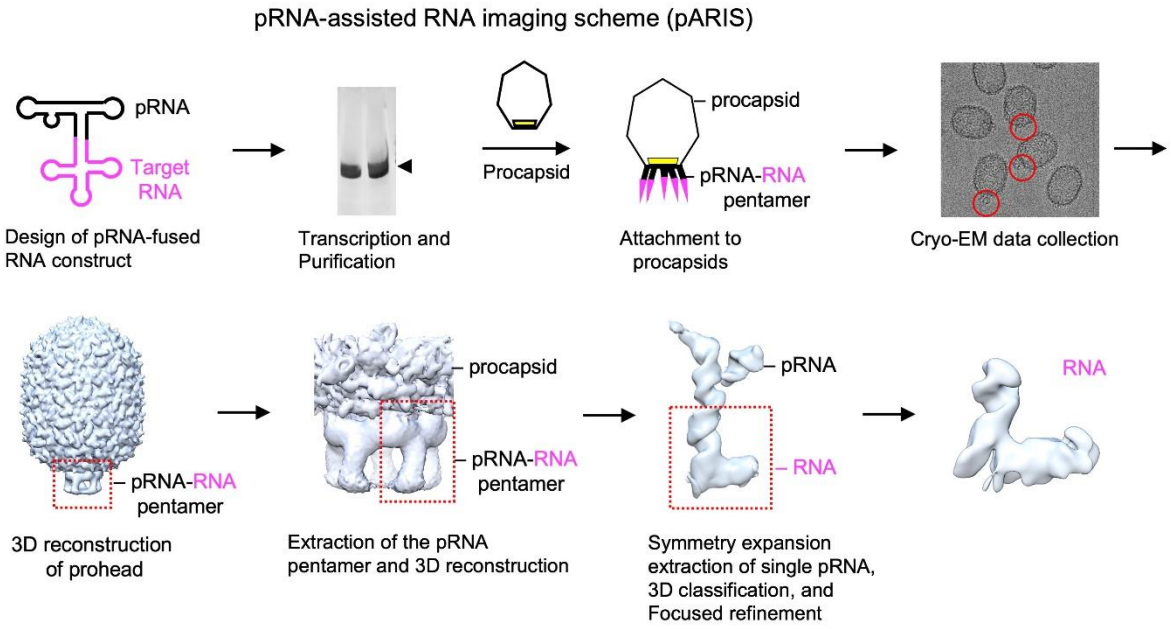


**Figure 1.** The pRNA-assisted RNA imaging scheme, pARIS. The overall workflow for pARIS is shown. The designed pRNA-fused target RNAs (pink) are generated by T7 RNA transcription. The purified pRNA-fused target RNAs are attached to Φ29 procapsids, applied to cryo-EM grids, and vitrified. Locations of some pRNAs are indicated by red circles in the cryo-EM image (upper right). Data collection and processing of the entire procapsid are first required to determine the position of the pRNA. Particles are then reextracted centered at the pRNA-fused RNA (red dashed box, bottom left). Following fivefold symmetry expansion, individual pRNA-fused RNAs are extracted, and nested focused refinement is used to obtain the structure of the target RNA.

### *3.2. Design of pRNA fusion constructs*

In double-stranded DNA (dsDNA) viruses, the genome is packaged into a preformed capsid, or procapsid, by a DNA packaging motor. In bacteriophage Φ29, this motor consists of the connector protein, pRNA, and the ATPase [16−18]. Five copies of pRNA assemble into a stable pentameric ring at this unique connector vertex [19,20]. The pRNA is 174 nt in length and consists of two conserved domains connected by a single-stranded linker (domain I comprises nt 1–117 and domain II nt 131–174) (Figure 2A) [28,29]. The minimal procapsid-binding region (nt 25–95) is sufficient to bind the procapsid and form the pentamer via intermolecular base pairing [21]. In pARIS, we exploit the modular architecture of pRNA by using this 71-nt segment as a scaffold to attach target RNAs (Figure 2).

We designed two types of pRNA constructs for assembly on procapsids: a wild-type (WT) pRNA and a circularly permuted pRNA (pRNAcp) (Figure 2B,C). The pRNA scaffold adopts a three-way

junction structure, with the 5′ and 3′ ends forming one arm of the junction. As a result, attachment of a target RNA at the 5′ or 3′ ends may allow rotation around the single bond between pRNA and the attached molecule, introducing unwanted flexibility. In the circularly permuted pRNAcp, the 5′ and 3′ ends were relocated to the procapsid-binding region (Figure 2B), reducing this flexibility while preserving the overall structure. Previous studies have shown that the circularly permuted pRNA functions similarly to the wild-type pRNA [22].

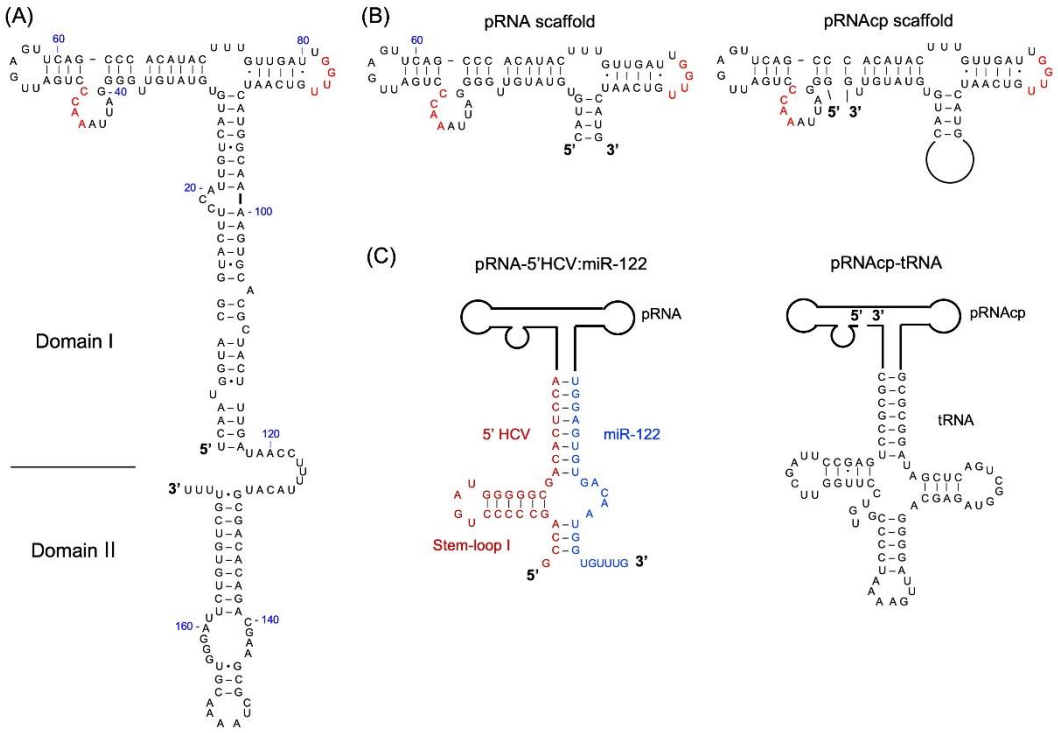


**Figure 2.** Design of pRNA-fused target RNA. (A) Structure of Φ29 pRNA. The 174 nt pRNA consists of two domains, I and II. Domain I contains the procapsid-binding and oligomerization regions. pRNA forms a pentameric ring on procapsids via complementary sequences (AACC and GGUU) between neighboring pRNA molecules (red). (B) Wild-type and circularly permuted pRNA scaffolds. The circularly permuted pRNA scaffold (pRNAcp) was designed by relocating the 5′ and 3′ termini of pRNA to the internal procapsid-binding region. (C) pRNA-fused target RNAs used in this study. The wild-type pRNA scaffold was used to attach the 5′ UTR of HCV and miR-122 sequences. The pRNAcp scaffold was used to insert the tRNA sequence.

Using these designs, we generated two pRNA-linked RNAs. In the first, a 70 nt tRNA was fused to the pRNAcp scaffold, preserving the 5′–3′ directionality (Figure 2C, right). In the second, sequences corresponding to the HCV 5′ UTR and miR-122 were appended to the 5′ and 3′ ends of the wild-type (WT) pRNA sequence, respectively (Figure 2C, left). The 5′ UTR of the HCV genome contains two miR-122 binding sites at its extreme 5′ end that are critical for viral replication [30−33]. The first miR-122 binding site has a higher affinity for miR-122 than the second, even though it is interrupted by a small stem-loop, stem-loop I (SLI). Thus, the miR-122 bound at the first site was chosen for structural studies in complex with the HCV 5′ UTR. The 5′ HCV sequence (29 nt) and the

miR-122 sequence (24 nt) were added to the 5′ and 3′ ends of the pRNA, respectively, without modification (Figure 2C). Importantly, both the tRNA (70 nt) and HCV: miR-122 complex (53 nt) are below the practical size limit for direct structural determination by cryo-EM.

*3.3. Cryo-EM reconstruction of pRNA-tRNA: Procapsid binding and initial cryo-EM reconstruction*

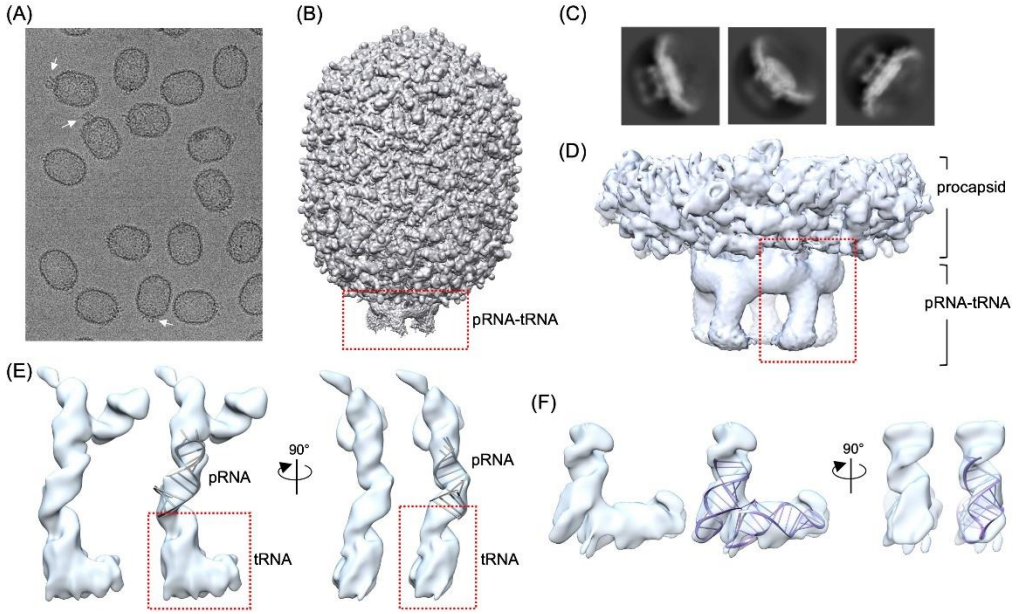


**Figure 3.** Structure determination of tRNA using pARIS. (A) Cryo-EM image of pRNA-fused tRNA assembled on Φ29 procapsids. Examples of procapsids with assembled pRNA-tRNA molecules are indicated by white arrows. (B) 3D reconstruction of Φ29 procapsids. The structure shows a well-defined capsid but poorly resolved pRNA-tRNA density. Density corresponding to the pRNA-tRNA pentamer is shown by a dashed red box. (C) 2D classes of reextracted Φ29 procapsids. Some views show the attached pRNA-tRNA molecules. (D) 3D reconstruction of the pentameric pRNA-tRNA assembly. Density corresponding to a single pRNA-tRNA subunit is shown by a dashed red box. (E) Structure of pRNA-fused tRNA. Each arm of the pentameric pRNA-tRNA assembly was isolated by subtracting the other four arms. (F) Structure of tRNA. The tRNA density was refined using a focused mask applied to the tRNA region, yielding a map in which the overall fold of the tRNA is resolved. A tRNA molecule (purple) is fitted into the density. Additional details of reconstruction are shown in Figure S1.

The pRNA-fused tRNA was generated by in vitro T7 RNA transcription and incubated with Φ29 procapsids at a 20:1 molar ratio (corresponding to a fourfold excess of pRNA pentamer). Cryo-EM images showed additional density at one end of the procapsid, indicating that the pRNA-tRNA construct had bound (Figure 3A). This result indicates that circular permutation of pRNA does not disrupt procapsid binding. The large size of Φ29 procapsids enabled robust automatic particle picking for downstream processing. Two-dimensional classification revealed a clear density corresponding to the pRNA-tRNA at the unique vertex of the procapsid. Reconstruction of the procapsid imposing fivefold symmetry yielded a 2.9 Å resolution map (Figure 3B). While density corresponding to the

pRNA-tRNA construct was visible, it was less well resolved, likely due to dominance of the procapsid signal during alignment. If the relative orientation of the pRNA-tRNA construct and the procapsid differed between different particles, densities corresponding to the pRNA-tRNA would not be aligned during the interparticle averaging inherent to 3D reconstruction.

### *3.4. Cryo-EM reconstruction of pRNA-tRNA: Focused reconstruction of pRNA-tRNA*

To address the poorly resolved pRNA-tRNA density, we used the orientation determined for each procapsid to recenter the box on the unique vertex where the pRNA pentamer is observed and reextracted the pRNA density into a smaller box (Figure 3C). The pRNA pentamer was reconstructed with fivefold symmetry imposed. Density corresponding to the tRNA moiety was clearly visible, extending from the pRNA procapsid-binding domain of the construct (Figure 3D). However, the low resolution of the resulting pRNA-tRNA pentamer suggested that each RNA molecule in the pentamer adopted a different relative orientation.

To further improve the resolution, individual arms of the pRNA pentamer were isolated by subtracting four of the five pRNA molecules from the C5 symmetry-expanded particles using a mask containing four pRNA molecules (4pRNA mask, Figure S1). This generated a particle stack corresponding to a single pRNA molecule with a fivefold increase in particle number. 3D classification and local refinement were then used to remove particles that did not show clear density for the tRNA. The resulting 3D reconstruction of the pRNA-tRNA was greatly improved, extending to 5.3 Å resolution, and the fold of the pRNA was clearly recognizable (Figure 3E). However, the density corresponding to the tRNA remained diffuse.

To better resolve the remaining tRNA density, we performed focused refinement on the tRNA using a mask that excluded density corresponding to the pRNA portion of the construct. Following 3D classification and local refinement, the final map containing the tRNA reached 4.8 Å resolution (Figure S1). At this resolution, the fold of the tRNA is clear. The good fit of a tRNA crystal structure into the cryo-EM map demonstrates that the procedure faithfully reconstructed the known structure of the tRNA (Figure 3F). These results demonstrate that pARIS enables visualization and accurate reconstruction of small RNAs, such as a 70-nt tRNA, that are otherwise difficult to resolve by cryo-EM.

### *3.5. Cryo-EM reconstruction of the 5′ HCV RNA and miR-122 complex using pARIS*

We next applied the pARIS approach to a biologically relevant RNA complex formed between the 5′ UTR of HCV and miR-122. The 5′ terminal region of the HCV genome and miR-122 form a complex that is required for efficient recruitment of viral polymerase and regulation of the switch between translation and genome replication [31,33−35]. As noted above, the 5′ HCV sequence contains the predicted stem-loop, SLI, that interrupts the miR-122 binding site (Figure 2C), raising the question of how miR-122 recognizes this structured HCV RNA with high affinity.

The HCV 5′ UTR and miR-122 sequences were appended to the 5′ and 3′ ends of pRNA, respectively, to preserve the native polarity of the complex (Figure 2C). As with the pRNA-tRNA construct, the pRNA-HCV: miR-122 complex was generated by in vitro T7 transcription and incubated with Φ29 procapsids at a 20:1 molar ratio (a fourfold excess of pRNA pentamer). Cryo-EM images of the particles showed additional density at one end of the procapsid, similar to that observed for the

pRNA-tRNA construct (Figure 4A). Density corresponding to the pRNA-HCV: miR-122 pentamer at the unique vertex of the procapsid was clearly visible in 2D class averages, indicating that extension of the 5′ and 3′ termini does not significantly disrupt procapsid binding.

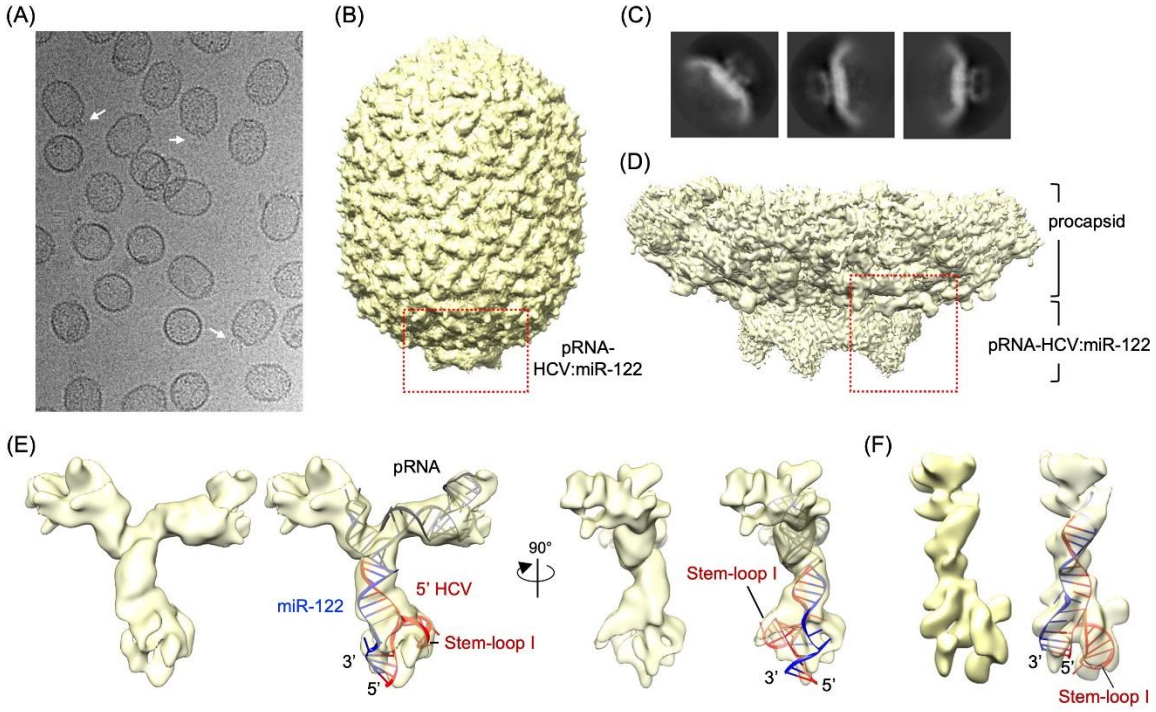


**Figure 4**. Structure determination of the 5′ HCV RNA and miR-122 complex using pARIS. (A) Cryo-EM image of the pRNA-fused HCV: miR-122 complex assembled on Φ29 procapsids. Examples of the procapsids with assembled pRNA-HCV: miR-122 molecules are indicated by white arrows. (B) 3D reconstruction of Φ29 procapsids. The structure shows a well-defined capsid but poorly resolved pRNA-HCV: miR-122 density. Density corresponding to the pRNA-HCV: miR-122 pentamer is shown by a dashed red box. (C) 2D classes of reextracted Φ29 procapsids. Some views show the attached pRNA-HCV: miR-122 molecules. (D) 3D reconstruction of the pentameric pRNA. Density corresponding to a single pRNA-HCV: miR-122 subunit is shown by a dashed red box. (E) Focused refinement of a single copy of the pRNA-fused HCV: miR-122 complex. A single copy of pRNA-HCV: miR-122 was used for focused refinement following C5 symmetry expansion. The fit of pRNA (PDB code 3R4F, grey) and the HCV: miR-122 complex (PDB code 7KI3) is shown on the right. The sequences corresponding to the 5′ UTR of HCV and miR-122 are shown in red and blue, respectively. (F) Structure of the HCV: miR-122 complex. The HCV: miR-122 density was refined using a focused mask applied to the RNA region. Additional details of reconstruction are shown in Figure S2.

Reconstruction of the procapsid resulted in a 3.7 Å resolution map (Figure 4B). However, as with the pRNA-tRNA construct, density corresponding to the pRNA-HCV: miR-122 construct was weak and diffuse, likely due to the dominance of the procapsid signal during alignment. Recentering at the pRNA vertex and reextraction into a smaller box, followed by 2D classification, showed that density corresponding to the pRNA-HCV: miR-122 pentamer was visible in some classes (Figure 4C).

Subsequent 3D reconstruction imposing fivefold symmetry resulted in a map in which density corresponding to the HCV: miR-122 region of the construct remained somewhat poor, suggesting that the HCV: miR-122 complex adopts different orientations in each pRNA leg (Figure 4D).

To resolve density corresponding to a single pRNA-HCV: miR-122 construct, a mask circumscribing four pRNA-HCV: miR-122 subunits (4pRNA mask) was created and used to subtract the density corresponding to four subunits, isolating a single subunit from the symmetry-expanded particles. 3D classification was then used to remove particles that did not show clear density for the HCV: miR-122 portion (Figure S2). Focused reconstruction of this single pRNA-HCV: miR-122 subunit produced a 6.9 Å resolution map that resolved the helical turn of the pRNA and the duplexed HCV and miR-122 (Figure 4E). Rigid-body fitting of the pRNA procapsid-binding domain (PDB code 3R4F) showed that the density for this region of the map agreed well with the known structure of the pRNA (Figure 4E). Fitting the previously determined crystal structure of the HCV: miR-122 complex bound to Argonaute2 (Ago2) (PDB: 7KI3) indicates that the density corresponding to the distal end of the complex is relatively diffuse (Figure 4E) [36].

Further 3D classification using a mask excluding pRNA density separated distinct conformational states of the HCV: miR-122 complex (Figure S2). Using the largest subset of particles with a consistent SLI orientation, focused refinement yielded a 6.7 Å reconstruction (Figure 4F). The lower resolution of the HCV: miR-122 reconstruction relative to the tRNA reconstruction likely reflects multiple factors. First, the initial procapsid reconstruction for the pRNA-HCV: miR-122 dataset reached lower resolution (3.7 Å versus 2.9 Å for pRNA-tRNA), limiting the accuracy of subsequent centering and alignment steps used to isolate the RNA density. Second, unlike the tRNA construct, which was inserted into the circularly permuted pRNA scaffold, the HCV and miR-122 sequences were appended to the 5′ and 3′ termini of wild-type pRNA, likely introducing additional flexibility at the termini. Finally, the HCV-miR122 complex is likely inherently more dynamic than the relatively rigid tRNA.

Together with previous studies showing that Ago2 stabilizes SLI, these results suggest that miR-122 alone, in the absence of Ago-2, is insufficient to stabilize SLI [36]. The observed flexibility of SLI suggests that this region is not rigidly constrained in the absence of protein binding partners. We therefore modeled the HCV: miR-122 complex as the duplex regions formed between the 5′ HCV RNA (nt 2-4 and 22-29) and miR-122 (nt 1-8 and 14-16), with SLI treated as a flexible element (Figure 4F). This model is consistent with the cryo-EM density and supports a mechanism in which flexibility at the 5′ end of the HCV genome allows miR-122 to bind efficiently without steric conflict from SLI. Comparison of the pARIS-derived model with the previously determined crystal structure (PDB: 7KI3) [36] suggests that the rigidity of SLI imposed by interactions with Ago2 is mechanistically important for stabilizing the HCV: miR-122 complex. In the context of Ago2, these interactions likely stabilize a specific SLI orientation, contributing to the protection of the viral genome from exonuclease activity.

## 4. Discussion

Determining structures of small-to-medium-sized RNAs (50–200 nt; ~16.5–66 kDa) remains a significant challenge. As RNA–RNA interactions are increasingly recognized as central to viral replication and host–pathogen interactions [37], methods that enable structural characterization of RNA-only complexes will become increasingly important. While advances in cryo-EM have enabled near-atomic resolution structures of large macromolecular assemblies, small RNAs remain difficult

targets because of their limited size and dynamic nature. Here, we developed pARIS as a scaffold-based approach to enable cryo-EM analysis of such RNAs by increasing their effective size and stabilizing their conformation through attachment to the Φ29 procapsid. This strategy provides several practical and conceptual advantages.

First, the well-established Φ29 system enables straightforward sample preparation, including pRNA attachment to procapsids and freezing for cryo-EM analysis. Unlike small RNAs, which often require extensive optimization of vitrification conditions to achieve suitable ice thickness and particle visibility, the procapsids are readily identifiable in cryo-EM images, simplifying grid screening and data acquisition.

Second, the pRNA scaffold stabilizes the attached RNA. By constraining the geometry of the fused construct, particularly at the 5′ and 3′ ends of a stem, the scaffold reduces conformational heterogeneity that would otherwise degrade reconstruction quality. The use of both WT and circularly permuted pRNA allows further flexibility in how target RNAs are incorporated, accommodating different structural contexts. For WT pRNA, the sequence of the target RNA extends from the 5′ and 3′ ends of the pRNA, ensuring the two ends are physically adjacent, thus allowing for correct base pairing and folding of the target RNA. The pRNAcp scaffold is well-suited for inserting stem-loop structures. Additionally, the pRNA scaffold provides selectivity for correctly folded target RNAs. If the pRNA or the RNA of interest does not fold correctly, the pRNA-linked RNA construct would not bind to the procapsid or assemble as a pentamer via intermolecular base pairing between adjacent pRNA procapsid-binding domains. Thus, pARIS selects for pRNA constructs that contain a higher population of correctly folded pRNA and target RNA, improving compositional homogeneity.

Third, the pRNA improves signal-to-noise ratio (SNR) by providing additional mass and facilitating particle picking. Due to their size and dynamic nature, small RNAs have low SNR for cryo-EM reconstructions, making particle picking extremely difficult. In pARIS, a target RNA is fused to a pRNA domain that assembles on procapsids. By virtue of being attached to these large procapsids, particle picking is greatly facilitated. In addition, low SNR makes filtering out poor particles at later stages of image processing difficult, negatively affecting the quality of 3D reconstruction. The pentameric form of the pRNA scaffold increases the signal of the RNA portion, allowing particles without the pRNA pentamer to be filtered out at early stages of the reconstruction procedure.

Finally, the pentameric pRNA-target RNA assembly on procapsids yields five individual copies of the RNA of interest per particle, thus increasing the total number of RNA particles by fivefold upon symmetry expansion. We observed that small RNA molecules often have preferred orientations, i.e., end-on views are rare. In contrast, Φ29 procapsids generally show a broader distribution of orientations, and thus the attached RNA molecules also show a broader distribution of orientations.

Here, we demonstrate this approach using two systems: a 70 nt (~23.1 kDa) tRNA and a 53 nt (~17.5 kDa) HCV 5′ UTR and miR-122 complex, resolved to 4.8 Å and 6.7 Å, respectively. At these resolutions, the overall RNA folds are well defined, enabling structural interpretation. While we focused here on relatively small RNAs, the modular nature of the pRNA scaffold should permit extension to larger constructs. It may also be possible to extend pARIS beyond the use of the procapsid. The pRNA sequence has previously been used to generate RNA origami structures [38−40], raising the possibility of designing scaffold-only assemblies that retain the advantages of multimerization while reducing particle size. Such approaches could increase particle density in micrographs and further improve data collection efficiency.

Recent scaffold-based approaches have demonstrated that attaching small flexible RNAs to larger

rigid RNA scaffolds can enable reasonably high-resolution structure determination of those small RNA targets [41−43]. These studies establish the considerable promise of scaffold-based cryo-EM for RNAs that are otherwise too small for conventional single-particle analysis. Although the current implementation of pARIS does not yet achieve the same resolution, it offers several distinct advantages. First, pARIS employs a relatively simple scaffold that does not require folding of a large catalytic RNA, simplifying construct design and sample preparation. Second, by exploiting the unique fivefold portal vertex of the Φ29 procapsid, each particle contributes five independently refinable RNA copies following symmetry expansion while simultaneously providing a large fiducial for particle alignment and orientation determination. These advantages are balanced by increased computational complexity, including signal subtraction, symmetry expansion, and focused refinement to isolate individual RNA copies. We anticipate that future improvements in scaffold rigidity, RNA attachment strategies, and image-processing methods will further improve the attainable resolution, allowing the higher symmetry of the pARIS architecture to be more fully exploited. Thus, these scaffold-based strategies should be viewed as complementary approaches that collectively broaden the applicability of cryo-EM to small and dynamic RNA molecules.

## Use of generative-AI tools declaration

ChatGPT (OpenAI) was used to assist with language editing of the manuscript. The authors take full responsibility for all scientific content and conclusions.

## Acknowledgements

This work was supported by NIH grants R01AI182321 (to MCM and PJJ), R01GM122979 (to MCM and PJJ), R01GM127365 (to MCM), R01AI087856 (to KHC), R21AI181621 (to KHC), and T32GM008280 (to SS). We would also like to acknowledge the Sealy Center for Structural Biology and Molecular Biophysics (SCSB) for support of the UTMB cryo-EM and computational core facilities.

## Conflict of interest

All authors declare no conflicts of interest in this paper.

## Author contributions

M.C.M. and K.H.C. conceived the study. S.S. processed the pRNA-HCV: miR-122 cryo-EM data, contributed to figure preparation, and assisted with manuscript writing. N.P. collected and processed the pRNA-tRNA cryo-EM data. K.H.C. also contributed to processing of the pRNA–tRNA data. W.Z. and P.J.J. contributed procapsid and pRNA reagents, and P.J.J. contributed to the conceptualization of the circularly permuted RNA strategy. M.C.M. and K.H.C. wrote and edited the manuscript with input from all authors. All authors read and approved the final manuscript.

## References


1. Carninci P, Kasukawa T, Katayama S, et al. (2005) The transcriptional landscape of the mammalian genome. *Science* 309: 1559–1563. https://doi.org/10.1126/science.1112014
2. Cheng J, Kapranov P, Drenkow J, et al. (2005) Transcriptional maps of 10 human chromosomes at 5-nucleotide resolution. *Science* 308: 1149–1154. https://doi.org/10.1126/science.1108625
3. Kapranov P, Cawley SE, Drenkow J, et al. (2002) Large-scale transcriptional activity in chromosomes 21 and 22. *Science* 296: 916–919. https://doi.org/10.1126/science.1068597
4. Lorenzi L, Chiu HS, Avila Cobos F, et al. (2021) The RNA Atlas expands the catalog of human non-coding RNAs. *Nat Biotechnol* 39: 1453–1465. https://doi.org/10.1038/s41587-021-00936-1
5. Pertea M, Shumate A, Pertea G, et al. (2018) CHESS: a new human gene catalog curated from thousands of large-scale RNA sequencing experiments reveals extensive transcriptional noise. *Genome Biol* 19: 208. https://doi.org/10.1186/s13059-018-1590-2
6. Cech TR (2012) The RNA worlds in context. *Cold Spring Harb Perspect Biol* 4: a006742. https://doi.org/10.1101/cshperspect.a006742
7. Cech TR, Steitz JA (2014) The noncoding RNA revolution-trashing old rules to forge new ones. *Cell* 157: 77–94. https://doi.org/10.1016/j.cell.2014.03.008
8. Miao Z, Westhof E (2017) RNA Structure: Advances and assessment of 3D structure prediction. *Annu Rev Biophys* 46: 483–503. https://doi.org/10.1146/annurev-biophys-070816-034125
9. van Rooij E, Kauppinen S (2014) Development of microRNA therapeutics is coming of age. *EMBO Mol Med* 6: 851–864. https://doi.org/10.15252/emmm.201100899
10. Ma H, Jia X, Zhang K, et al. (2022) Cryo-EM advances in RNA structure determination. *Signal Transduct Target Ther* 7: 58. https://doi.org/10.1038/s41392-022-00916-0
11. Jackson RW, Smathers CM, Robart AR (2023) General strategies for RNA X-ray crystallography. *Molecules* 28: 2111. https://doi.org/10.3390/molecules28052111
12. Lee E, Bujalowski PJ, Teramoto T, et al. (2021) Structures of flavivirus RNA promoters suggest two binding modes with NS5 polymerase. *Nat Commun* 12: 2530. https://doi.org/10.1038/s41467-021-22846-1
13. Pujari N, Saundh SL, Acquah FA, et al. (2021) Engineering crystal packing in RNA structures I: Past and future strategies for engineering RNA packing in crystals. *Crystals (Basel)* 11: 952. https://doi.org/10.3390/cryst11080952
14. Gottipati K, McNeme SC, Tipo J, et al. (2023) Structural basis for cloverleaf RNA-initiated viral genome replication. *Nucleic Acids Res* 51: 8850–8863. https://doi.org/10.1093/nar/gkad618
15. Tipo J, Gottipati K, Slaton M, et al. (2024) Structure of HIV-1 RRE stem-loop II identifies two conformational states of the high-affinity Rev binding site. *Nat Commun* 15: 4198. https://doi.org/10.1038/s41467-024-48162-y
16. Cao S, Saha M, Zhao W, et al. (2014) Insights into the structure and assembly of the bacteriophage 29 double-stranded DNA packaging motor. *J Virol* 88: 3986–3996. https://doi.org/10.1128/JVI.03203-13
17. Hill AC, Bartley LE, Schroeder SJ (2016) Prohead RNA: a noncoding viral RNA of novel structure and function. *Wiley Interdiscip Rev RNA* 7: 428–437. https://doi.org/10.1002/wrna.1330
18. Simpson AA, Tao Y, Leiman PG, et al. (2000) Structure of the bacteriophage phi29 DNA packaging motor. *Nature* 408: 745–750. https://doi.org/10.1038/35047129

19. Morais MC, Koti JS, Bowman VD, et al. (2008) Defining molecular and domain boundaries in the bacteriophage phi29 DNA packaging motor. *Structure* 16: 1267–1274. https://doi.org/10.1016/j.str.2008.05.010
20. Woodson M, Pajak J, Mahler BP, et al. (2021) A viral genome packaging motor transitions between cyclic and helical symmetry to translocate dsDNA. *Sci Adv* 7: eabc1955. https://doi.org/10.1126/sciadv.abc1955
21. Ding F, Lu C, Zhao W, et al. (2011) Structure and assembly of the essential RNA ring component of a viral DNA packaging motor. *Proc Natl Acad Sci USA* 108: 7357–7362. https://doi.org/10.1073/pnas.1016690108
22. Zhang C, Trottier M, Guo P (1995) Circularly permuted viral pRNA active and specific in the packaging of bacteriophage phi 29 DNA. *Virology* 207: 442–451. https://doi.org/10.1006/VIRO.1995.1103
23. Grimes S, Anderson D (1997) The bacteriophage phi29 packaging proteins supercoil the DNA ends. *J Mol Biol* 266: 901–914. https://doi.org/10.1006/JMBI.1996.0843
24. Zhao W, Morais MC, Anderson DL, et al. (2008) Role of the CCA bulge of prohead RNA of bacteriophage o29 in DNA packaging. *J Mol Biol* 383: 520–528. https://doi.org/10.1016/j.jmb.2008.08.056
25. Punjani A, Rubinstein JL, Fleet DJ, et al. (2017) cryoSPARC: algorithms for rapid unsupervised cryo-EM structure determination. *Nat Methods* 14: 290–296. https://doi.org/10.1038/nmeth.4169
26. Sanchez-Garcia R, Gomez-Blanco J, Cuervo A, et al. (2021) DeepEMhancer: a deep learning solution for cryo-EM volume post-processing. *Commun Biol* 4: 874. https://doi.org/10.1038/s42003-021-02399-1
27. Emsley P, Lohkamp B, Scott WG, et al. (2010) Features and development of Coot. *Acta Crystallogr D Biol Crystallogr* 66: 486–501. https://doi.org/10.1107/s0907444910007493
28. Morais MC (2012) The dsDNA packaging motor in bacteriophage o29, *Advances in Experimental Medicine and Biology*, Boston: Springer, 511–547. https://doi.org/10.1007/978-1-4614-0980-9_23
29. Wichitwechkarn J, Bailey S, Bodley JW, et al. (1989) Prohead RNA of bacteriophage phi 29: size, stoichiometry and biological activity. *Nucleic Acids Res* 17: 3459–3468. https://doi.org/10.1093/nar/17.9.3459
30. Henke JI, Goergen D, Zheng J, et al. (2008) microRNA-122 stimulates translation of hepatitis C virus RNA. *EMBO J* 27: 3300–3310. https://doi.org/10.1038/emboj.2008.244
31. Jopling CL, Yi M, Lancaster AM, et al. (2005) Modulation of hepatitis C virus RNA abundance by a liver-specific microRNA. *Science* 309: 1577–1581. https://doi.org/10.1126/science.1113329
32. Li Y, Yamane D, Masaki T, et al. (2015) The yin and yang of hepatitis C: synthesis and decay of hepatitis C virus RNA. *Nat Rev Microbiol* 13: 544–558. https://doi.org/10.1038/nrmicro3506
33. Scott S, Li Y, Bermek O, et al. (2023) Binding of microRNA-122 to the hepatitis C virus 5' untranslated region modifies interactions with poly(C) binding protein 2 and the NS5B viral polymerase. *Nucleic Acids Res* 51: 12397–12413. https://doi.org/10.1093/nar/gkad1000
34. Chahal J, Gebert LFR, Gan HH, et al. (2019) miR-122 and ago interactions with the HCV genome alter the structure of the viral 5' terminus. *Nucleic Acids Res* 47: 5307–5324. https://doi.org/10.1093/nar/gkz194

35. Schult P, Roth H, Adams RL, et al. (2018) microRNA-122 amplifies hepatitis C virus translation by shaping the structure of the internal ribosomal entry site. *Nat Commun* 9: 2613. https://doi.org/10.1038/s41467-018-05053-3
36. Gebert LFR, Law M, MacRae IJ (2021) A structured RNA motif locks Argonaute2:miR-122 onto the 5' end of the HCV genome. *Nat Commun* 12: 6836. https://doi.org/10.1038/s41467-021-27177-9
37. Damas ND, Fossat N, Scheel TKH (2019) Functional interplay between RNA viruses and nnon-coding RNA in mammals. *Noncoding RNA* 5: 7. https://doi.org/10.3390/ncrna5010007
38. Guo S, Tschammer N, Mohammed S, et al. (2005) Specific delivery of therapeutic RNAs to cancer cells via the dimerization mechanism of phi29 motor pRNA. *Hum Gene Ther* 16: 1097–1110. https://doi.org/10.1089/hum.2005.16.1097
39. Hao Y, Kieft JS (2014) Diverse self-association properties within a family of phage packaging RNAs. *RNA* 20: 1759–1774. https://doi.org/10.1261/rna.045948.114
40. Li H, Zhang K, Pi F, et al. (2016) Controllable self-assembly of RNA tetrahedrons with precise shape and size for cancer targeting. *Adv Mater* 28: 7501–7507. https://doi.org/10.1002/adma.201601976
41. Haack DB, Rudolfs B, Jin S, et al. (2025) Scaffold-enabled high-resolution cryo-EM structure determination of RNA. *Nat Commun* 16: 880. https://doi.org/10.1038/s41467-024-55699-5
42. Jones CP, Ferre-D'Amare AR (2026) Scaffolds with optimized quaternary symmetry for de novo cryoEM structure determination of small RNAs. *Nat Methods* 23: 609–616. https://doi.org/10.1038/s41592-026-03016-x
43. Langeberg CJ, Kieft JS (2023) A generalizable scaffold-based approach for structure determination of RNAs by cryo-EM. *Nucleic Acids Res* 51: e100. https://doi.org/10.1093/nar/gkad784


AIMS Press